Chapter

The Investigation on the Fabrication and Characterization of the Multicomponent Ceramics Based on PZT and the Relaxor PZN-PMnN Ferroelectric Materials

Le Dai Vuong, Vo Thanh Tung and Phan Dinh Gio

Abstract

This chapter presents the investigation of fabrication and the physical properties of the $Pb(Zr_{1-x}Ti_x)O_3$-$Pb(Zn_{1/3}Nb_{2/3})O_3$-$Pb(Mn_{1/3}Nb_{2/3})O_3$ multicomponent ceramics. The multicomponent $yPb(Zr_{1-x}Ti_x)O_3$-$(0.925 - y)Pb(Zn_{1/3}Nb_{2/3})O_3$-$0.075Pb(Mn_{1/3}Nb_{2/3})O_3$ (PZT-PZN-PMnN) ceramics were synthesized by conventional solid-state reaction method (MO) combined with the B-site oxide mixing technique (BO). Research results show that the electrical properties of PZT-PZN-PMnN ceramics are optimal at a PZT content of 0.8 mol and Zr/Ti ratio of 48/52. At these contents, the ceramics have the following optimal properties: electromechanical coupling factor, k_p = 0.62 and k_t = 0.51; piezoelectric constant (d_{31}) of 130 pC/N; mechanical quality factor (Q_m) of 1112; dielectric loss (tan δ) of 0.005; high remanent polarization (P_r) of 30.4 μC.cm^{-2}; and low coercive field (E_C) of 6.2 kV.cm^{-1}. Investigation of the domain structure of the two ferroelectric phases (tetragonal and rhombohedral) in the ZnO-doped PZT-PZN-PMnN with compositions at near the morphotropic phase boundary is described as follows: the 90 and 180° domains exist in the tetragonal phase, while the 71, 109, and 90° domains are located in the rhombohedral phase, and the widths of these domains were about 100 nm. Besides, the ceramics exhibited excellent temperature stability, which makes them a promising material for high-intensity ultrasound applications.

Keywords: ceramics, the multicomponent ceramics, PZT-PZN-PMnN, ZnO nanoparticles, the ultrasonic transducers

1. Introduction

Over the years, piezoelectric materials have been heavily investigated for ultrasonic device applications. Of the many piezoelectric materials, $Pb(Zr_{1-x}Ti_x)O_3$ (PZT)-based materials are more attractive for these applications, such as piezoelectric actuators, ultrasonic motors, and piezoelectric transformers [1–9].

As $Pb(Mn_{1/3}Nb_{2/3})O_3$ (PMnN), $Pb(Zn_{1/3}Nb_{2/3})O_3$ (PZN) have been found to be promising ferroelectric ceramics with good piezoelectric characteristics, high Curie temperature, they meet well with the requirements of ultrasonic transducer applications [6–8]. They are ferroelectric materials that have characteristics such as: high dielectric constant, the temperature at the phase transition point between the ferroelectric and paraelectric phase is broad (the diffuse phase transition), and a strong frequency dependency of the dielectric properties [6, 10–12]. The PZT-PZMnN ceramics, as one of PZT-$Pb(B', B'')O_3$ solid solutions, received more attention due to their high piezoelectric properties [6, 10–14]. So far, the sintering temperature of PZT-based ceramics is usually too high, approximately 1200°C [9]. To improve the sinterability and properties of lead piezoelectric ceramics, on the basis of the conventional solid phase sintering method, various advanced manufacturing techniques have been applied to the fabrication of lead ceramics such as the two-stage calcination method [15], high energy mill [16] and liquid phase sintering [9, 15, 17–20], hot isostatic pressing, hot pressing, microwave sintering, and spark plasma sintering [17] has been used effectively. Among them, the liquid phase sintering is a simple and effective method of improving the properties of PZT-based ceramics, which is currently attracting the interests of many scientists [15, 16]. By using various additives, such as NiO, B_2O_3, Bi_2O_3, Li_2CO_3, $BiFeO_3$, ZnO, CuO, and Bi_2O_3, many researchers have successfully decreased the sintering temperature of PZT-based ceramics [5, 6, 13, 14, 18–23]. We also attempted decreasing sintering temperatures from 1150 to 930°C, which significantly improved the electrical properties of the ceramics. In these ceramics, Li_2CO_3 is considered as a liquid-phase sintering aid [5, 21, 24]. The addition of Li_2CO_3 improved the sinterability of the $Bi_{0.5}(Na_{0.8}K_{0.2})_{0.5}TiO_3$ ceramic samples and caused an increase in the density and grain size at a sintering temperature of 1100°C [19]. With increasing Li_2CO_3 content, the phase structure of the ceramics changed from rhombohedral to tetragonal, indicating that it is close to the morphotropic phase boundary (MPB) of this system.

In this chapter, in order to develop the composition ceramics for high-intensity ultrasound applications, xPb($Zr_yTi_{(1-y)}$)O_3-(0.925-x)Pb($Zn_{1/3}Nb_{2/3}$)O_3-0.075Pb($Mn_{1/3}Nb_{2/3}$)O_3 (PZT-PZN-PMnN) ceramics were fabricated by the B-site oxide mixing technique. The aim of the chapter was, first, to carry out a phase formation, piezoelectric, ferroelectric, and dielectric characteristics in a solid solution of PZT-PZN-PMnN. The compositions synthesized in this study were x = 0.65, 0.70, 0.75, 0.80, 0.85, and 0.90 in the ternary system, xPb($Zr_{0.47}Ti_{0.53}$)O_3-(0.925 – x)Pb($Zn_{1/3}Nb_{2/3}$)O_3-0.075Pb($Mn_{1/3}Nb_{2/3}$)O_3. Then detailed systematic structural analysis and the study of physical properties were carried out for x = 0.8 compositions by varying the value of y in the Zr/Ti ratio. This will help to better determine how variations in the phase content affect local atomic arrangements and hence the electrical properties; and, second, to study the effect of ZnO nanoparticles on the sintering behavior and electrical properties of 0.8Pb($Zr_{0.48}Ti_{0.52}$)O_3-0.125Pb($Zn_{1/3}Nb_{2/3}$)O_3-0.075Pb($Mn_{1/3}Nb_{2/3}$)O_3 piezoelectric materials; the application, fabrication of ultrasonic transducers are reported and discussed.

2. Synthesis of PZT-PZN-PMnN ceramics by the B-site oxide mixing technique

Lead-based mixed B-site cation perovskites of $(B', B'')O_3$-type exhibit diffuse phase transition (DPT) behaviors of broad dielectric constant spectra in contrast to the sharp phase transitions of Pb(Zr,Ti)O_3 and $PbTiO_3$ [25]. The complex perovskite compounds are difficult to synthesize by conventional solid-state

reaction method owing to the formation of pyrochlore phases and reduction of desirable properties, such as the electromechanical coupling factor and dielectric constant, which originate from the perovskite structure [25]. The B-site oxide mixing technique (BO) [26, 27] (formation of a B-site precursor of $(B', B'')O_2$-type, followed by a reaction with PbO) has been applied to several complex perovskite compositions and the results are quite successful [22, 28, 29]. In the conventional method (MO), oxide powders of PbO, ZrO_2, TiO_2, ZnO, MnO_2, and Nb_2O_5 were weighed and milled for 8 h. To identify the temperature for calcining PZT-PZN-PMnN, we investigated the data of thermal gravimetric (TG) and thermal analysis (DTA) of PZT-PZN-PMnN powder (**Figure 1**). As per the above results, the TG curve exhibits a linear decrease in the total mass of the studied powder. However, the DTA curve shows an endothermic peak from 739 to 840°C, corresponding to the ion evaporation. To ensure the phase creation in the sample, the mixture powder was calcined at temperatures a little higher than 850°C after being milled for 8 h and pressed into pellets [30]. Afterward, the calcined PZT-PZN-PMnN pellets were continued to be milled for 16 h and pressed into disk 12 mm in diameter and 1.5 mm in thick under 100 Tan/cm^2.

In the B-site oxide mixing technique, in order to identify the temperature for calcining of $(Zn,Mn)Nb_2(Zr,Ti)O_6$ (BO), we investigated the data for thermal gravimetric (TG) and thermal analysis (DTA) of $(Zn,Mn)Nb_2(Zr,Ti)O_6$ powders, as shown in **Figure 2**. As per results, the TG curve of the mixture powder shows that the total mass of the studied powder decreases linearly. However, the DTA curve shows the endothermic peak at 978°C, corresponding to the temperature of powder evaporation. In order to ensure that the temperature is at least above 978°C for each powder grain, the mixture powder was calcined at little higher temperature of 1100°C [6, 11, 21, 22] after the powders of BO and PbO were weighed and milled for 8 h.

The powders were calcined at a temperature of 850°C for 2 h, producing the PZT-PZN-PMnN compound. The samples were sintered at 950°C for 2 h. **Figure 3** shows the X-ray diffraction (XRD) patterns of the PZT-PZN-PMnN ceramics prepared by different methods. From X-ray diagrams, we can see that the BO sample has only pure perovskite phase with rhombohedral structure, and this was determined by the (*200*) diffraction peak observed near 44° with no splitting. As seen in **Figure 4**, the BO sample was almost fully dense, and the average grain size of the

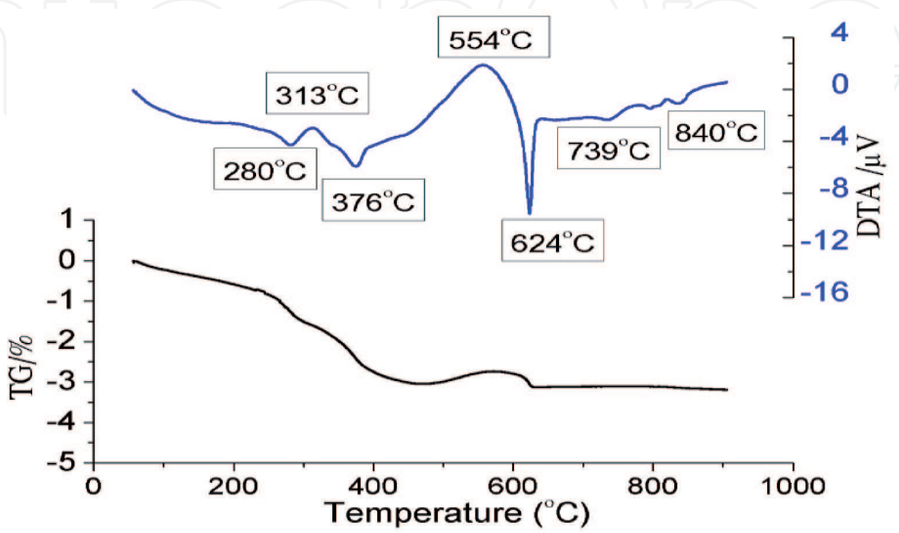

Figure 1.
TG/DTA curves for the powder mixture compositions.

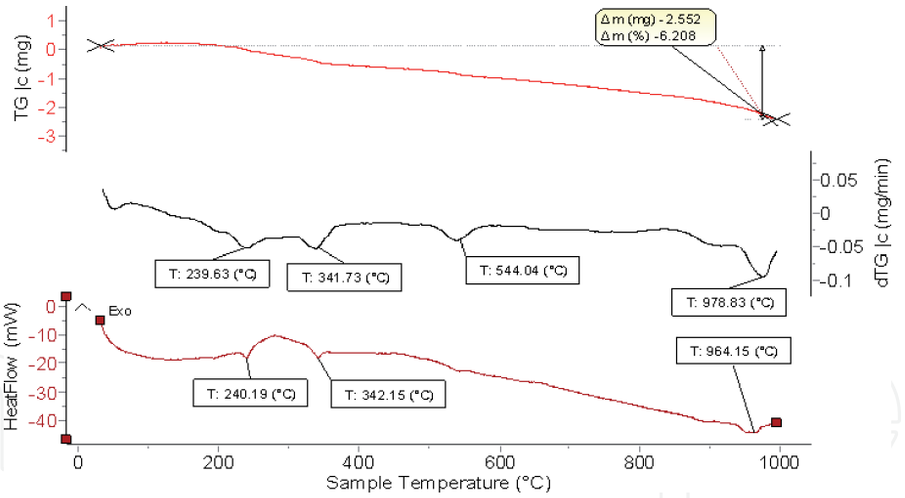

Figure 2.
TG and DTA curves of $(Zn,Mn)Nb_2(Zr,Ti)O_6$ power at 10°C/min heating rate.

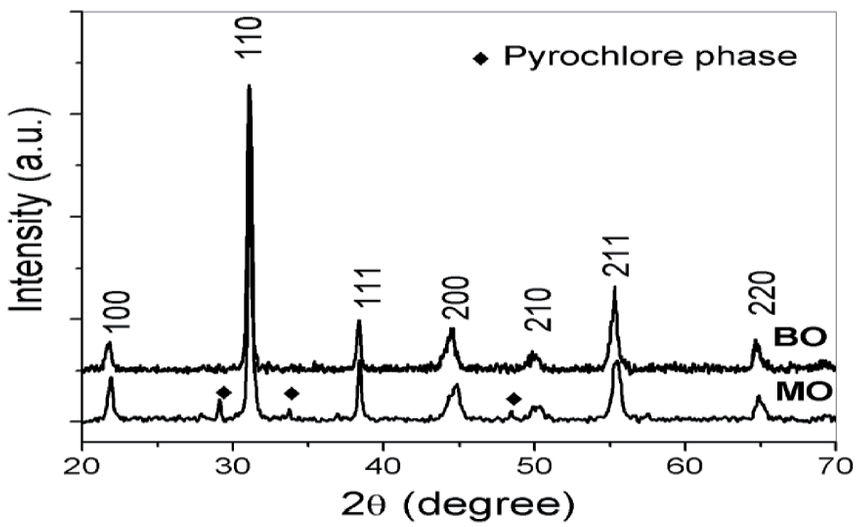

Figure 3.
X-ray diffraction diagram of the BO and MO samples.

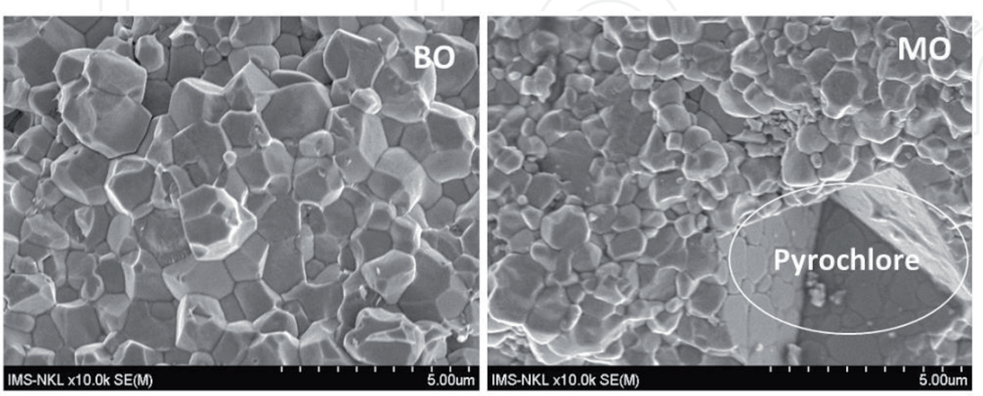

Figure 4.
Microstructures of BO and MO samples.

sample was large. However, in the MO sample, besides the perovskite phase with rhombohedral structure (**Figure 3**), there is a small pyrochlore phase. This is in good accordance with the microstructure (**Figure 4**). It is said that formation of the

pyrochlore phase may be due to the steric and electrostatic interaction between the high polarization of the Pb^{2+} cation and the B-sites cation (Zn^{+2}, Nb^{+5}) [24, 27, 31].

3. Characterization of ceramics

The crystalline structure of the sintered ceramics was analyzed by X-ray diffraction (XRD) analysis at room temperature. The surface morphology was examined using field emission scanning electron microscopy (SEM), X-ray energy dispersive spectra (EDS) was measured using a Hitachi S-3400N scanning electron microscope with an EDS system Thermo Noran, and the densities of the ceramic samples were measured by the Archimedes method from the ceramic samples weighed in air, in water and the density of water. The grain size is determined from SEM micrographs by a linear intercept method. The dielectric properties of ceramics (relative dielectric constant and dielectric loss) were measured with a HIOKI 3532 impedance analyzer. The electromechanical coupling factors k_p, k_t and piezoelectric constant (d_{31}) were determined by the resonance method according to the IEEE Standard 61 using an impedance analyzer Agilent 4196B and RLC HIOKI 3532 [32, 33]. The ferroelectric properties were measured by applying the Sawyer-Tower method [34].

4. The effects of $Pb(Zr_{0.47}Ti_{0.53})O_3$ on the structure, microstructure, and the dielectric properties of $xPb(Zr_{0.47}Ti_{0.53})O_3$-$(0.925 - x)$ $Pb(Zn_{1/3}Nb_{2/3})O_3$-$0.075Pb(Mn_{1/3}Nb_{2/3})O_3$ ceramics

Lead-zinc niobate $Pb(Zn_{1/3}Nb_{2/3})O_3$ (PZN) materials were first synthesized in the 1960s [35, 36]. It is one of the well-known relaxor perovskite ferroelectrics exhibiting a diffused phase transition with a phase transition temperature around 140°C (T_m) [6, 12]. However, pure perovskite lead-zinc niobate ceramics are relatively difficult to prepare by conventional solid-state reaction method [37]. The addition of other perovskite materials such as $PbTiO_3$, $BaTiO_3$, and $PbZr_{0.47}Ti_{0.53}O_3$ (PZT) is necessary to stabilize the perovskite structure for PZN ceramics [12, 25, 38, 39]. The B-site ions in the PZT perovskite structure (Zr^{4+}, Ti^{4+}) might have been partially substituted by the B-site ions of the relaxor-type PZN structure (Zn^{2+}, Nb^{5+}), which allowed the PZT-PZN solid-solution system to retain the perovskite structure and the high sinterability of lead-based relaxor ceramics [12, 25, 38, 39]. Based on the preparation of pyrochlore-free $Pb(Ni_1/_3Nb_2/_3)O_3$ (PNN), Vittayakorn et al. [40] studied the effects of PZT contents on the dielectric and ferroelectric properties of 0.5PNN-$(0.5 - x)$ PZN-xPZT ceramics. The results showed that the dielectric constant (ε_r), the remanent polarization (P_r), and Curie temperature (T_c) increase with the increase in PZT content. With the combination of the preeminent properties between PZT, PZN, and PMnN, the PZT-PZN solid-solution systems hope to achieve the prominent properties of normal ferroelectric PZT and relaxor ferroelectric PZN and PMnN, which could exhibit better piezoelectric and dielectric properties simultaneously. In this section, in order to improve electrical properties, we have prepared xPZT-$(0.925 - x)$PZN-0.075PMnN ceramics with the content of PZT from 0.65 to 0.90. The $xPb(Zr_yTi_{(1-y)})O_3$-$(0.925 - x)Pb(Zn_{1/3}Nb_{2/3})O_3$–$0.075Pb(Mn_{1/3}Nb_{2/3})O_3$ ceramic samples have been fabricated by the B-site oxide mixing technique as described in Section 2.

Figure 5 shows XRD patterns of the PZT-PZN-PMnN ceramics at various contents of PZT. As observed, all ceramics have pure perovskite phase with dominantly

tetragonal structure. The lattice parameters (a, c) of the samples have been evacuated from the (002) and (200) peaks of diffraction patterns, which are shown in the inset of **Figure 5**. When PZT content increases, the tetragonality c/a ratio increases. According to the $PbZrO_3$-$PbTiO_3$ phase diagram, $Pb(Zr_{0.47}Ti_{0.53})O_3$ is the tetragonal phase (space group P4mm) near the morphotropic phase boundary region at room temperature (RT) [41, 42]. While $Pb(Mn_1/_3Nb_2/_3)O_3$ is a cubic structure and the PZN composition was determined to be the rhombohedral (space group R3m) [36, 38]. Therefore, with increasing the molar fraction of PZT, the crystal symmetry of the PZT-PZN-PMnN should change due to the tetragonal distortions of PZT [6, 25, 40]. In order to determine what chemical composition of the PZT-PZN-PMnN ceramic changes during sintering, the EDS analysis is performed and is shown in **Figure 6**. The presence of lithium (Li) is not plotted here because its atomic number is low and the mass percentage is too small [43]. **Table 1** also showed the comparison in the mass of Pb, Zr, Ti, Nb, Zn, and Mn elements between before and after sintering of the PZT-PZN-PMnN ceramics. It is quite clear that the chemical composition of the synthesized ceramic obtained by EDS analysis can roughly accord with

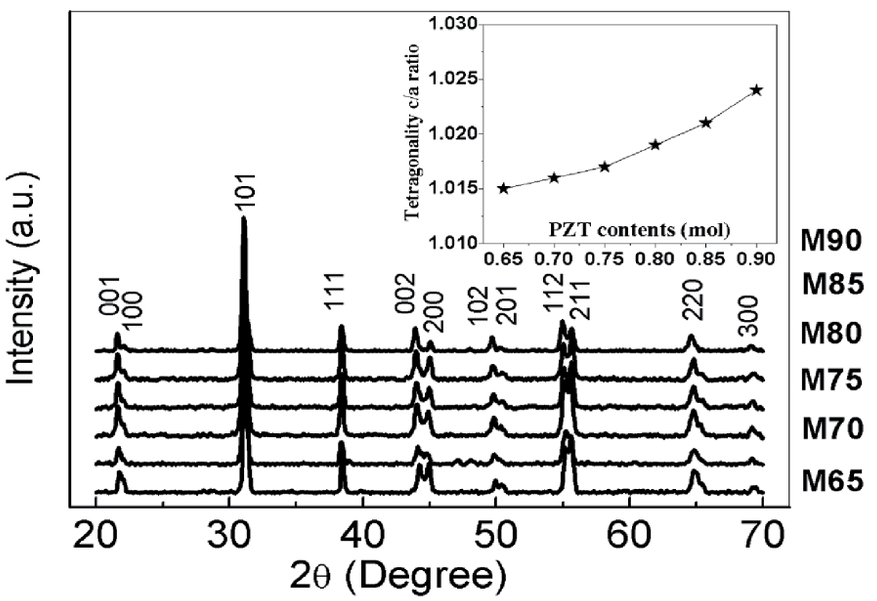

Figure 5.
XRD patterns of PZT-PZN-PMnN ceramics at various contents of PZT.

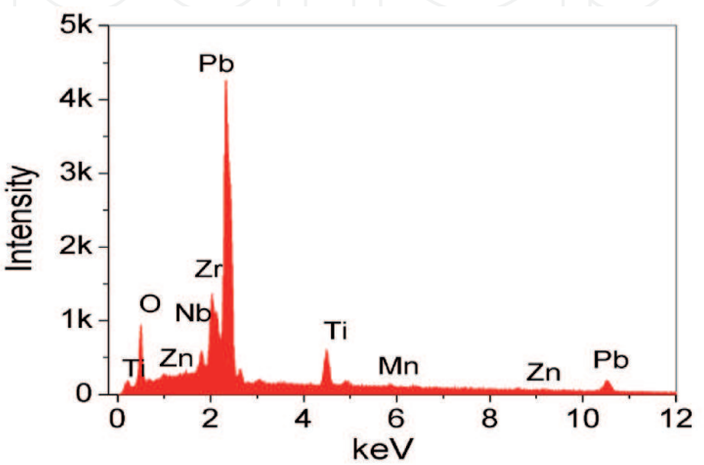

Figure 6.
EDS spectrum of 0.8PZT-0.125PZN-0.075PMnN ceramics.

Elements	The mass percentage of elements from the precursors	Mass percentage of elements from the synthesized ceramic
Pb	64.4	57
Zr	10.72	10.24
Ti	6.10	4.97
Nb	3.79	3.06
Zn	0.83	0.59
Mn	0.42	0.43

Table 1.
The chemical composition of the PZT-PZN-PMnN ceramics.

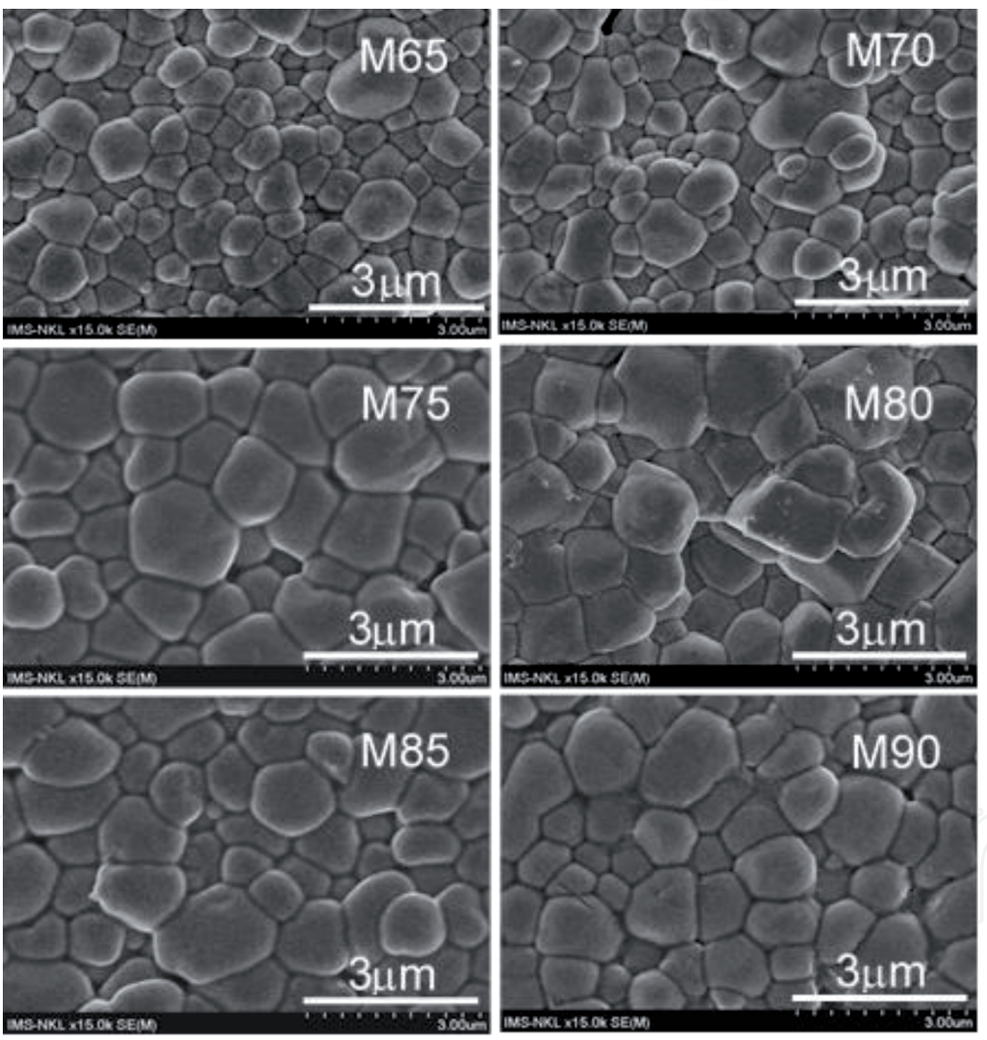

Figure 7.
Surface morphologies observed by the SEM of PZT-PZN-PMnN ceramics at various contents of PZT.

the general formula of the material without Pb. The reason could be explained by the evaporation of PbO during sintering [6, 25, 31]. Therefore, it is necessary to add excess 5 wt% PbO to compensate for lead loss during sintering.

Figure 7 shows microstructures of the PZT-PZN-PMnN ceramics at various contents of PZT. The average grain size of these samples is increased with the increase of PZT content in **Table 2**. On the other hand, the average grain size is reduced when x increases above 0.8. These results are obviously consistent with the change in the density of PZT content of PZT-PZN-PMnN ceramics, as shown in **Table 2**.

Samples	M65	M70	M75	M80	M85	M90
Average grain size (μm)	0.56 ± 0.02	0.66 ± 0.02	0.90 ± 0.02	1.04 ± 0.01	0.85 ± 0.02	0.83 ± 0.03
The average density of ceramics (g/cm^3)	7.77 ± 0.02	7.78 ± 0.01	7.80 ± 0.01	7.81 ± 0.01	7.72 ± 0.01	7.69 ± 0.02

Table 2.
The average grain size of PZT-PZN-PMnN ceramics.

Table 2 shows the density of the PZT-PZN-PMnN ceramics as a function of the PZT content. With the increase of PZT content up to 0.8, the mass density of PZT-PZN-PMnN ceramics increases. It achieves a maximum value (ρ = 7.81 g/cm^3, 96% of the theoretical density in which the theoretical density of ceramic is calculated using Eq. (1):

$$\rho = \frac{nA}{V_C N_A} \tag{1}$$

where n = number of atoms associated with each unit cell in ABO_3, A = atomic weight, V_C = volume of the unit cell in ABO_3, and N_A = Avogadro's number.

This is explained by the content of PZT was added to the ceramic system is less than 0.8 mol, a large number of pores were present, indicating insufficient densification of the sample (**Figure 7**: some SEM for M70, M90 are missing and M75 is not good). As the PZT content increases, the ceramics became denser, and the sample was almost fully dense at a PZT content of 0.8 mol.

The PZT content dependence of the dielectric constant (ε_r), dielectric loss (tan δ), and mass density (ρ) of the PZT-PZN-PMnN ceramics at 1 kHz and RT is illustrated in **Figure 8**. It can be seen that dielectric properties are strongly influenced by the composition of the ceramics. When the content of PZT increases from 0.65 to 0.8 mol, values of ε_r increase and reach to the maximum of 1230 at 0.8 mol of PZT. Then, these rapidly decrease with increasing x, while tan δ decreases with increasing PZT content. The minimum tan δ of 0.005 is obtained at x = 0.8 and then increased. It could be explained by the combination of a large and homogeneous grain size and the highest densification for the composition of 0.8PZT-0.125PZN-0.075PMnN ceramic [22].

In order to characterize the dielectric loss of all samples, the measurement of dielectric constant dependent on temperature is carried out at 1 kHz, as shown in **Figure 8**. With increasing PZT content, the dielectric constant peak increases and becomes sharpened. Hence, the material properties change from relaxor ferroelectricity to normal ferroelectricity. The permittivity and the maximum temperature (T_m) of the ceramics are shown in **Figure 9**. It shows that the T_m increases with increasing PZT content and is in the range of 206–275°C. There is a difference between the phase transformation temperatures of PZN (T_m ~ 140°C) [36, 38, 40] and PZT (T_C ~ 390°C) [25, 35], so it is significant to study the dependence of phase transition temperature of the PZT-PZN-PMnN ceramics on PZT content [40]. When the temperature is higher than T_m, the function $\varepsilon(T)$ is out of order the Curie-Weiss law in the normal ferroelectric materials. The fact the relationship between dielectric constant (ε) and temperature (T) above T_m can be complied by the modified Curie-Weiss law for analyzing of experimental data [44] is shown as follows:

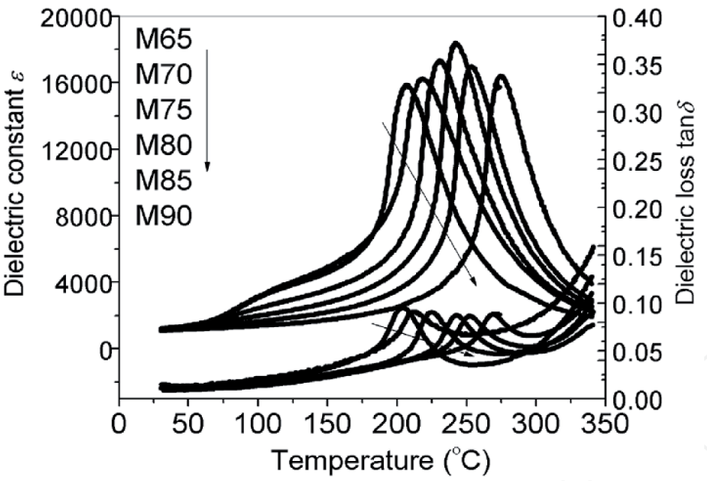

Figure 8.
Temperature dependence of the dielectric constant and dielectric loss tan δ at 1 kHz of samples.

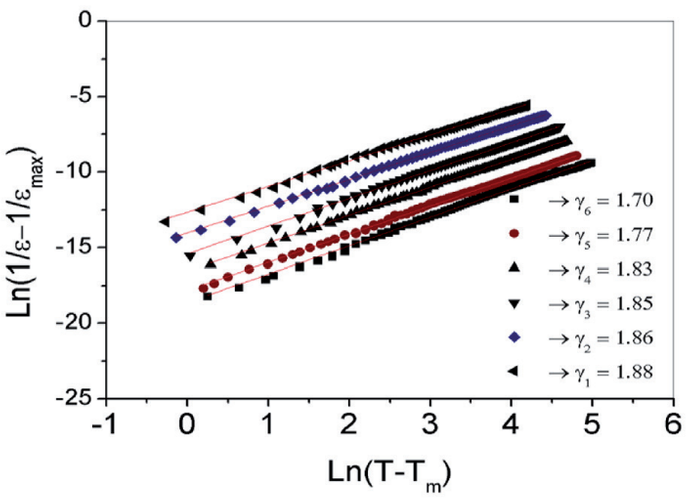

Figure 9.
The plot of ln(1/ε – 1/$ε_m$) versus ln(T-T_m) of PZT-PZN-PMnN ceramics at 1KHz.

$$\frac{1}{\varepsilon}-\frac{1}{\varepsilon_{\max}}=\frac{\left(T-T_m\right)^{\gamma}}{C'} \tag{2}$$

where C is the modified Curie–Weiss constant and γ is the diffuseness exponent, which changes from 1 to 2 for normal ferroelectrics to fully disorder relaxor ferroelectrics, respectively [44].

The slopes of the fitting curves (**Figure 9**) are used to determine the γ value of xPZT-(0.925 – x)PZN-0.075PMnN ceramics at 1 kHz. As can be seen in **Figure 9**, the γ changes from 1.70 to 1.88. Thus, it is indicated that the transitions are of a diffuse type and the ceramics are highly disordered.

To analyze the frequency dependence of T_m, it is necessary to use Vogel-Fulcher law [6, 45]:

$$F = f_o \exp\left(-T_o / \left(T - T_f\right)\right) \tag{3}$$

$$Ln\left(f\right) = f_o - T_o\left(T_m - T_f\right) \tag{4}$$

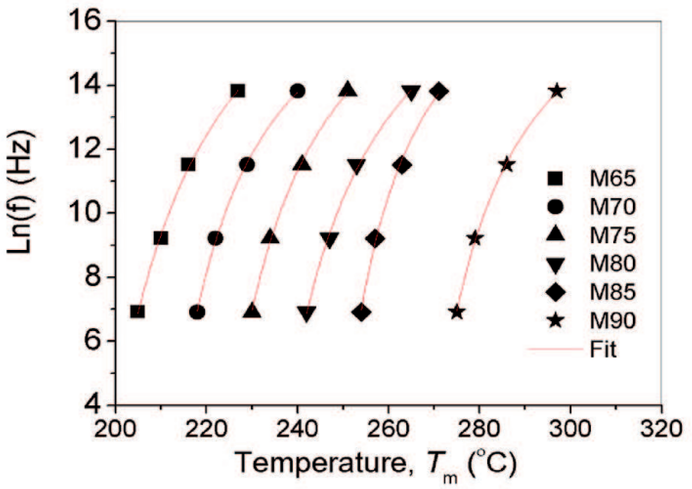

Figure 10.
The plot of ln(f) versus T_m as a function of the measured frequency of PZT-PZN-PMnN.

Samples	M65	M70	M75	M80	M85	M90
T_0 (°C)	398	254	302	331	217	253
T_f (°C)	179	198	208	218	237	255

Table 3.
The value of fitting parameters to Vogel-Fulcher relationship.

where T_f is the freezing temperature, E_a is the activation energy for polarization fluctuation of a polar nanoregion, f_o is a characteristic frequency or Debye frequency, and k_B is the Boltzmann constant = 1.38×10^{23} J/K, and $T_o = E_a/k_B$. **Figure 10** shows the plot of $\ln(f)$ versus T_m as a function of the measured frequency of PZT-PZN-PMnN. The symbols are the experimental points, and the line is the corresponding fitting to the Vogel-Fulcher relationship as listed in **Table 3**.

5. The effects of Zr/Ti ratio on the structure, microstructure, and the electrical properties of $0.8Pb(Zr_yTi_{1-y})O_3$–$0.125Pb(Zn_{1/3}Nb_{2/3})O_3$–$0.075Pb(Mn_{1/3}Nb_{2/3})O_3$ ceramics

The influence of Zr/Ti ratio on the structure of PZT-PZN-PMnN ceramics has been analyzed through the X-ray diffraction patterns (**Figure 11**). The patterns reveal a pure perovskite phase for all ceramic samples.

As can be seen, the tetragonality of PZT-PZN-PMnN ceramics decreased with increasing Zr/Ti ratio content through the c/a ratio decreases. According to Dixit et al. [46] and Kahoul et al. [47], the morphology of $Pb(Zr,Ti)O_3$ ceramics is strongly dependent on the Zr and Ti content. The content of the rhombohedral phase gradually increases within decreasing the Zr content simultaneously, and the tetragonal phase gradually decreases. The morphological evolution with Zr contents in this work may be attributed to the increase of a rhombohedral phase in these ceramics [46, 47]. This may be because the large Zr^{+4} (0.86 Å) ions diffuse into the PZT-PZN-PMnN lattice to replace Ti^{4+} (0.61 Å), resulting in the increase in the lattice constant and a shift in the XRD peak position toward lower 2θ values, similar to our recent research [48].

Effects of the contents of Zr/Ti ratio on the microstructure development of the ceramics are shown in **Figure 12**. In general, surface ceramics with large grains and

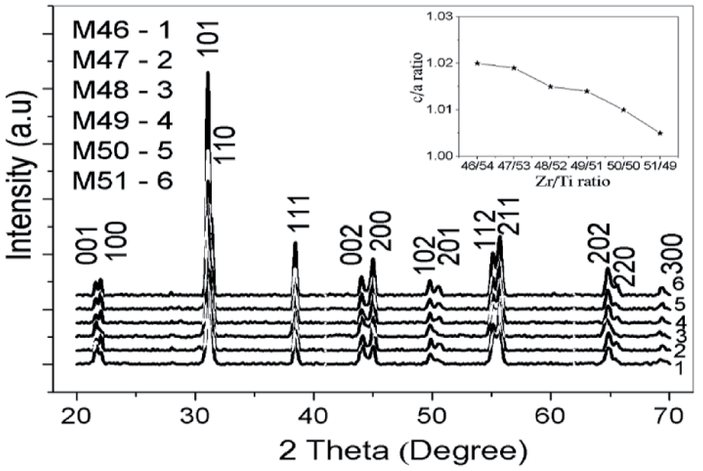

Figure 11.
X-ray diffraction patterns of ceramics with different Zr/Ti ratio contents: M46 (Zr/Ti = 46/54), M47 (Zr/Ti = 47/53), M48 (Zr/Ti = 48/52), M49 (Zr/Ti = 49/51), M50 (Zr/Ti = 50/50), and M51 (Zr/Ti = 51/49).

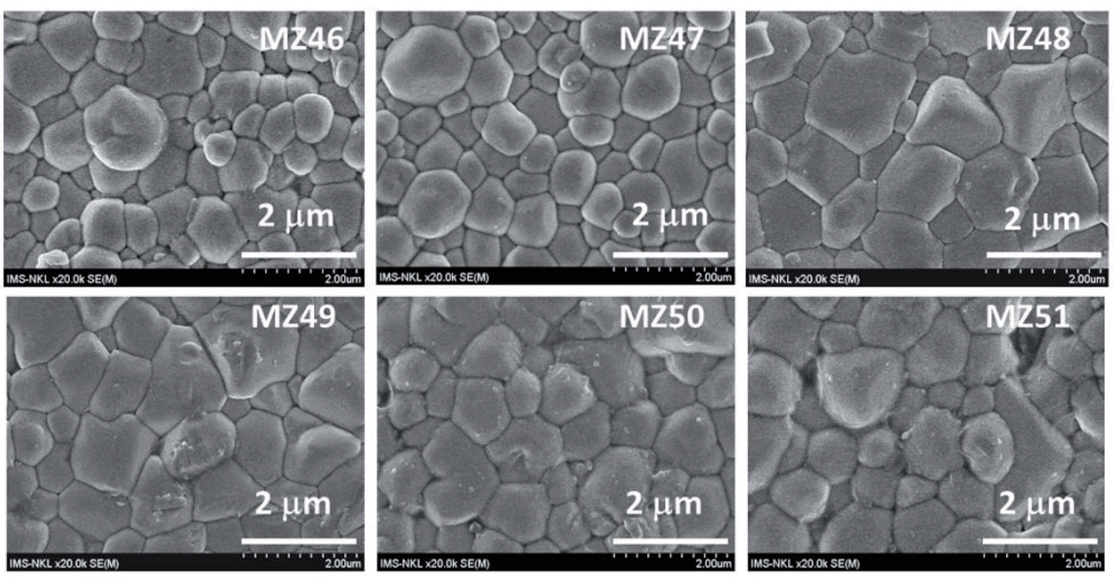

Figure 12.
Microstructures of samples with the different Zr/Ti ratio contents: MZ46 (Zr/Ti = 46/54), MZ47 (Zr/Ti = 47/53), MZ48 (Zr/Ti = 48/52), MZ49 (Zr/Ti = 49/51), MZ50 (Zr/Ti = 50/50), and MZ51 (Zr/Ti = 51/49).

uniform microstructure were obtained in all samples, and the average grain size of samples is increased with the increasing content of Zr/Ti ratio. In conformity with the previous densification results, highly dense samples exhibited high degrees of grain close packing. However, some pores and abnormal grain boundaries were observed in **Figure 12** (MZ50 and MZ51) and the average grain size is reduced.

Figure 13 shows the temperature dependence of ε and tan δ of the ceramic samples measured at different frequencies (1 kHz–1 MHz). It can see that with the increase in Zr amount, the T_m temperature of ceramics decreases as indicated in **Figure 14**. This may explain that the Curie temperature of $PbZrO_3$ ceramics is about 232°C [25], and it is lower than that of $PbTiO_3$ ceramics, 490°C [49, 50]. It is due to the decrease of lattice parameters and bond lengths [46, 47].

In order to determine the piezoelectric properties of ceramics, resonant vibration spectra of the PZT-PZN-PMnN samples were measured at room temperature (**Figure 15**), and from these resonant spectra, the piezoelectric parameters of the samples, such as electromechanical coefficients k_p, piezoelectric coefficients d_{31}, mechanical quality coefficient Q_m, and dielectric loss tan δ were determined (**Figure 16**).

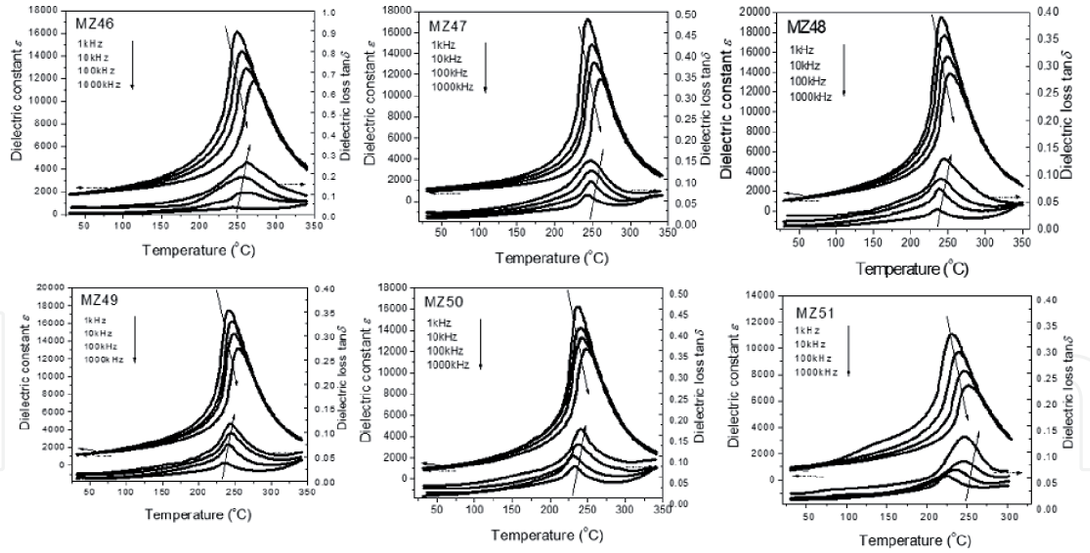

Figure 13.
Temperature dependence of relative dielectric constant ε and dielectric loss tan δ of samples at different frequencies: MZ46 (Zr/Ti = 46/54), MZ47 (Zr/Ti = 47/53), MZ48 (Zr/Ti = 48/52), MZ49 (Zr/Ti = 49/51), MZ50 (Zr/Ti = 50/50), and MZ51 (Zr/Ti = 51/49).

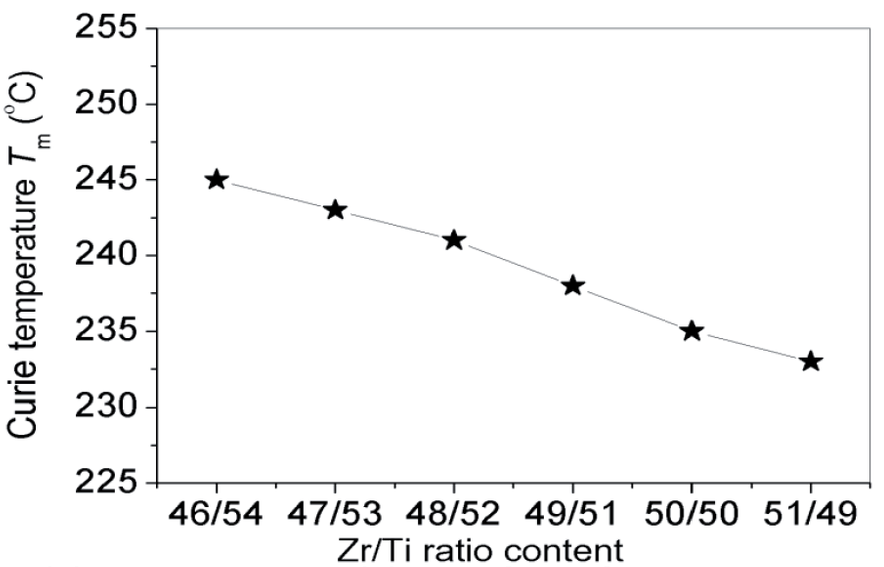

Figure 14.
The Curie temperature T_m *of PZT-PZN-PMnN ceramics with different amounts of Zr/Ti ratio.*

It can be observed that the k_p, d_{31}, Q_m, and tan δ depend on the amount of the Zr/Ti ratio content. The piezoelectric properties of ceramics are markedly improved. The following optimized values were obtained at Zr/Ti = 48/52, k_p = 0.62, d_{31} = 140 pC N^{-1}, Q_m = 1112, and tan δ = 0.005. This fact can be explained by the increased grain size effect and better modification of microstructure in ceramics [10, 25, 49, 50]. However, with the further increasing the Zr/Ti ratio content, the electrical properties of PZT-PZN-PMnN ceramics are reduced. The cause is due to an abnormal grain boundary, and the average grain size is also reduced, as shown in **Figure 12**.

The *P-E* hysteresis loops of PZT-PZN-PMnN at room temperature are displayed in **Figure 17(a)**, and P_r and E_c are presented in **Figure 17(b)**. With the increase in P_r and the decrease in E_c, the ferroelectric properties of PZT-PZN-PMnN ceramics improve. With increasing of Zr/Ti ratio content, the value of P_r increases and reaches the highest value of 34.5 μC/cm^2) at the Zr/Ti ratio of 48/52, and then decreases. The coercive field E_C decreases slightly with the increasing of Zr/Ti ratio content and reaches the smallest value of 9.0 kV/cm at Zr/Ti ratio of 48/52.

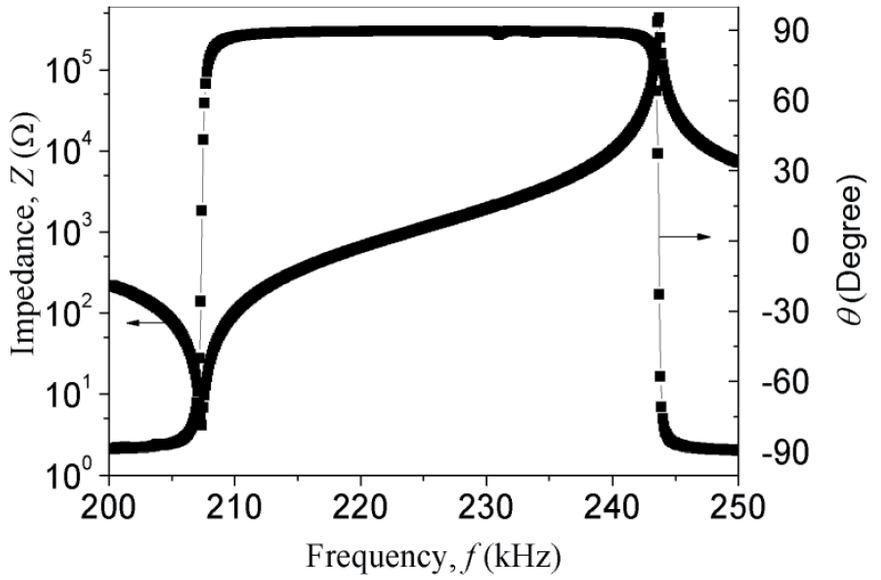

Figure 15.
The spectrum of radial resonance of MZ48 sample (at room temperature).

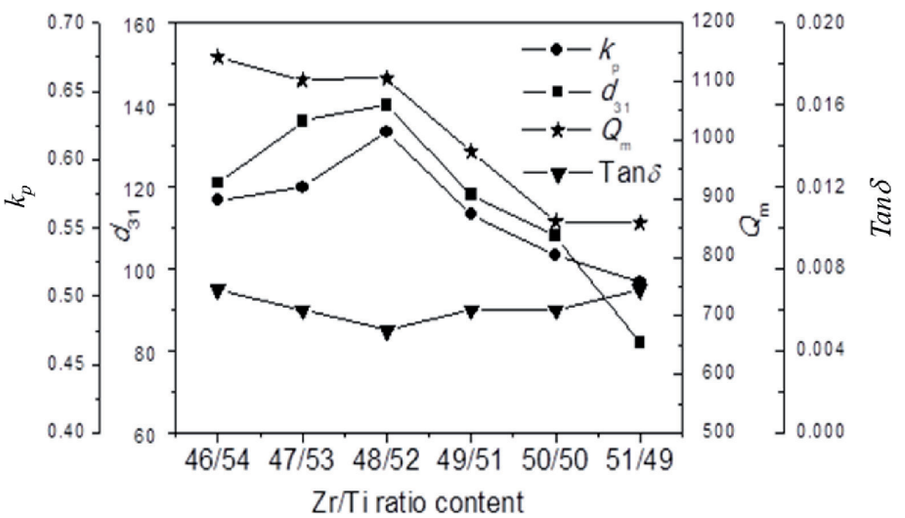

Figure 16.
The values of k_p, d_{31}, Q_m, *and tan* δ *of the PZT-PZN-PMnN ceramic samples.*

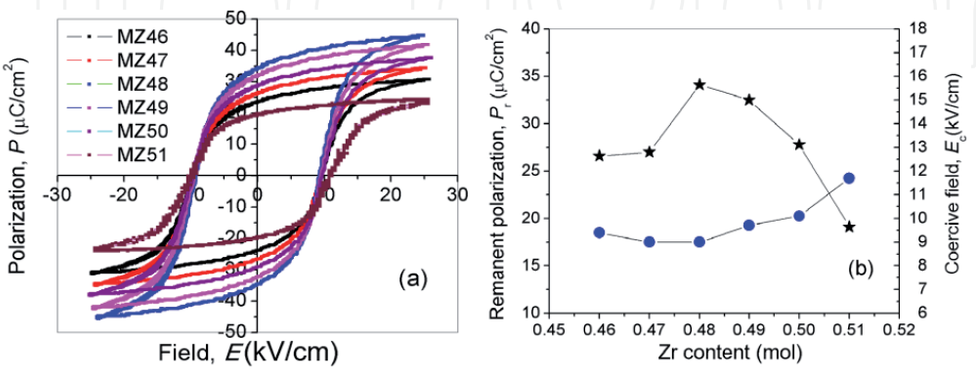

Figure 17.
(a) Hysteresis loops of samples and (b) P_r *and* E_c *as a function of Zr/Ti ratios.*

The effect of temperature on the ferroelectric properties of ceramics was studied by the hysteresis loops of the $0.8Pb(Zr_{0.48}Ti_{0.52})O_3–0.125Pb(Zn_{1/3}Nb_{2/3})O_3–0.075Pb(Mn_{1/3}Nb_{2/3})O_3$ sample in the temperature range of 30–280°C

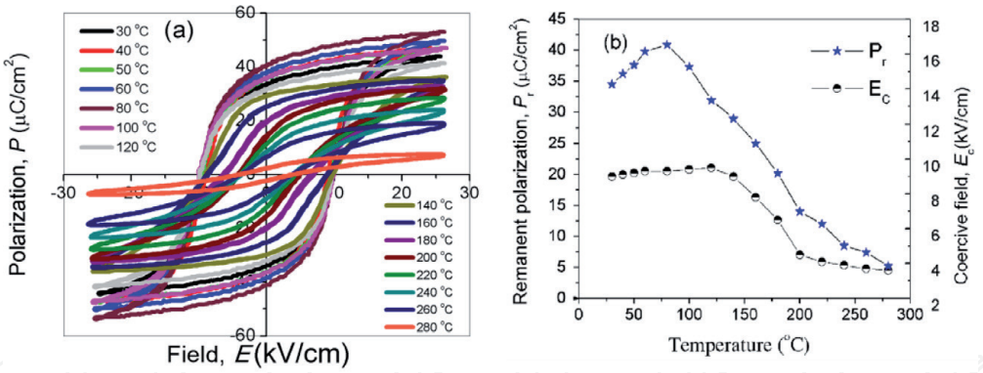

Figure 18.
(a) Hysteresis loops and (b) temperature dependence of P_r and E_C of MZ48 sample at a different temperature.

(**Figure 18(a)**). The hysteresis loops of the ceramics exhibited excellent temperature stability due to the broad diffusive phase transition between the nonergodic and ergodic relaxor states that coexisted over a wide temperature range [51]. When the temperature increased from room temperature to 120°C, the remanent polarization and the coercive field increased (**Figure 18(b)**). The reason is when the temperature increases, the oxygen vacancies in the perovskite structure will move and significantly increase the conductivity of the material, which should increase the dielectric loss. However, when the temperature rises above 120°C, the remanent polarization P_r and the coercive field E_c decreased (**Figure 18(b)**). Generally, the size of the hysteresis loops depends on the dielectric loss of the material and the metastable macro-domain structure and the immobilizations of the domain walls [52]. Therefore, when the temperature increased, large thermal motion energy caused an increase in bipolar disorder, narrowed the hysteresis loops, and decreased the remanent polarization and the coercive field. In addition, the hysteresis loops showed that the P_r is nonzero at T_m but decays to zero at temperatures above T_m. These results are consistent with the literature [40].

6. Ferroelectric domain structures around the morphotropic phase boundary of the $0.8Pb(Zr_{0.48}Ti_{0.52})O_3$-$0.125Pb(Zn_{1/3}Nb_{2/3})O_3$-$0.075Pb(Mn_{1/3}Nb_{2/3})O_3$ ceramics

In this section, in order to develop the composition ceramics for high-intensity ultrasound applications, $0.8Pb(Zr_{0.48}Ti_{0.52})O_3$–$0.125Pb(Zn_{1/3}Nb_{2/3})O_3$–$0.075Pb(Mn_{1/3}Nb_{2/3})O_3$ + z wt% ZnO nanoparticles ceramics were fabricated by the B-site oxide mixing technique with the variations of z and then the phase formation, piezoelectric and dielectric characteristics were investigated with the variations of z. The general formula of the studied materials is $0.8Pb(Zr_{0.48}Ti_{0.52})O_3$–$0.125Pb(Zn_{1/3}Nb_{2/3})O_3$–$0.075Pb(Mn_{1/3}Nb_{2/3})O_3$ + z wt% ZnO, where z = 0.0, 0.20, 0.25, 0.30, 0.35, 0.40, and 0.45. The obtained ZnO nanoparticles are spherical in shape, with their average diameter about 27 nm [9, 18]. On the other hand, reagent-grade oxide powders of PbO, ZnO, MnO_2, Nb_2O_5, ZrO_2, and TiO_2 (purity ≥99%) were used as starting raw materials for the fabrication of the PZT-PZN-PMnN ceramics.

Figure 19 shows X-ray diffraction patterns of the PZT-PZN-PMnN ceramics at various contents of ZnO nanoparticles. All the compositions have demonstrated pure perovskite phases and no trace of the second phase. Further XRD analysis is performed in the 2θ ranges from 43 to 46°, as shown in the inset of **Figure 19**. It can be seen that a phase transformation from the rhombohedral structure to the tetragonal structure occurs with increasing ZnO content. The samples with z = 0.0 and 0.2

have the rhombohedral structure characterized by a peak $(200)_R$ at $2\theta \approx 44.5°$. With z = 0.40 and 0.45, the ceramics exist as a tetragonal phase which is indicated by the splitting of $(002)_T$ and $(200)_T$ peaks in the 2θ range from 44 to 45° [23, 53, 54]. In the z range from 0.25 to 0.35, the ceramics coexist as rhombohedral and tetragonal phase, which is revealed by the coexistence of $(002)_T$, $(200)_T$, and $(200)_R$ peaks. Therefore, it could be said that the composition z from 0.25 to 0.35 is close to the morphotropic phase boundary (MPB) of this system. The phenomenon can be explained by the penetration of Zn^{2+} ions into the grains to substitute for B-site ions due to the similar radii of Zn^{2+} (0.074 nm), Ti^{4+} (0.0605 nm), Zr^{4+} (0.072 nm), and Nb^{5+} (0.064 nm) at the octahedral sites of the perovskite lattice, forming additional anionic vacancies. This causes a distortion in the lattice; therefore, the substitution of Zn^{2+} ions at Ti^{4+} or Zr^{4+} sites caused the c-axis to be lengthened and changed in lattice parameters and degree of tetragonality (c/a). These results are consistent with the literature [5, 19, 21, 48, 55].

Effects of the contents of ZnO nanoparticles on the microstructure development of the ceramics are shown in **Figure 20**. As can be described in the microstructure of

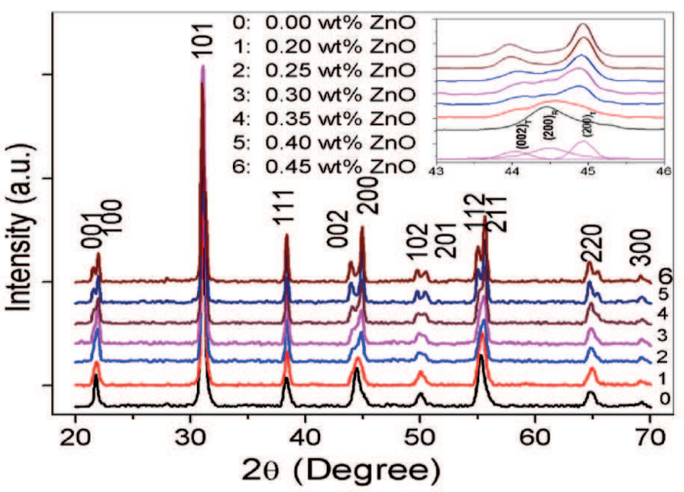

Figure 19.
X-ray diffraction patterns of PZT-PZN-PMnN ceramics at various contents of ZnO nanoparticles [9].

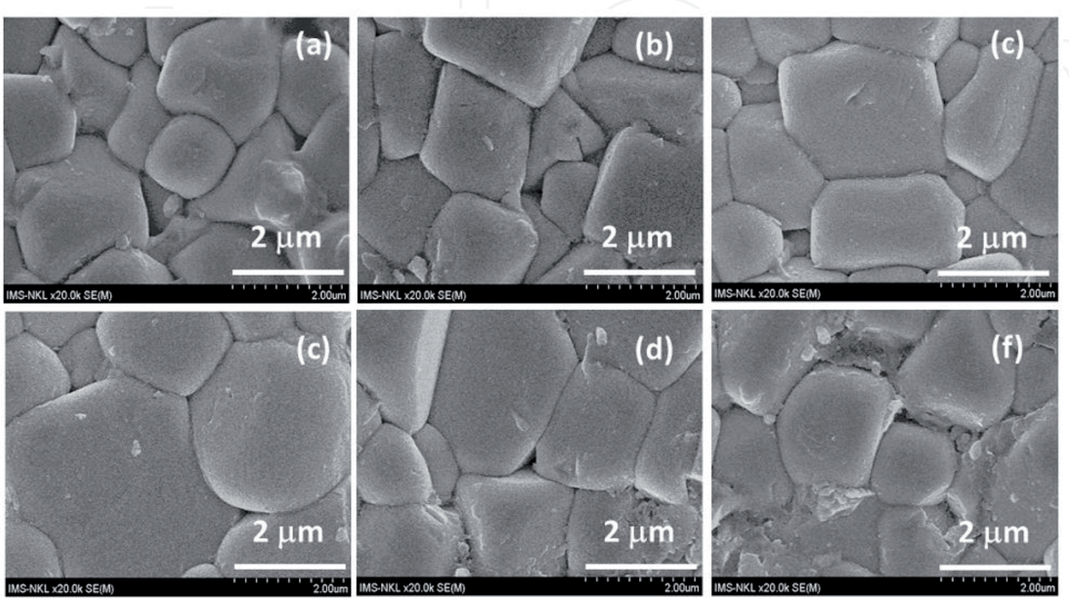

Figure 20.
Microstructures of PZT-PZN-PMnN ceramics at different contents of ZnO nanoparticles: (a) 0.20 wt%, (b) 0.25 wt%, (c) 0.3 wt%, (d) 0.35 wt%, (e) 0.40 wt%, and (f) 0.45 wt%.

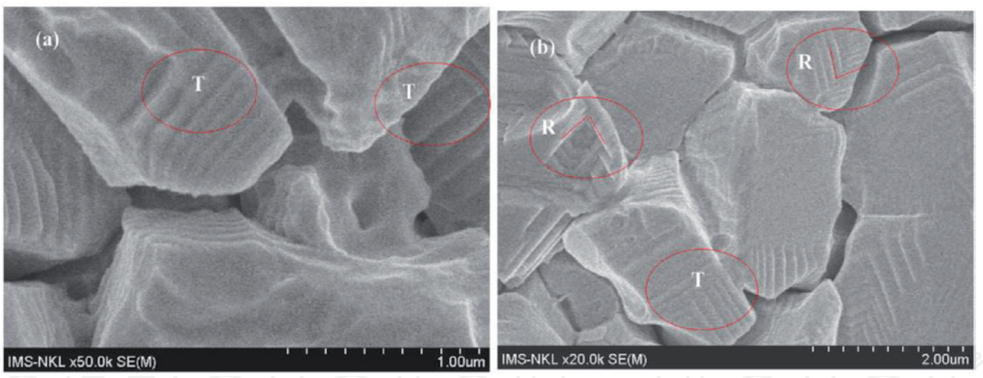

Figure 21.
The domain structures micrographs of the PZT-PZN-PMnN ceramics; (a) 0.4 wt% ZnO; (b) 0.35 wt% ZnO [9].

ceramics, the grain size of PZT-PZN-PMnN samples is increased with the increasing content of ZnO nanoparticles. This may explain that the low melting point of ZnO nanoparticles is beneficial to generate eutectic liquid phase at low temperature, and it can act as lubrication during the sintering process, wetting solid particles and providing capillary pressure between them, thus resulting in faster grain growth of PZT-PZN-PMnN ceramics [56, 57]. However, when the ZnO concentration is large, it exceeds the solubility limit of ZnO into the ceramics, and they will be located at grain boundaries preclude the grain growth process, as shown in **Figure 20(d)–(f)**.

Figure 21 shows evolution examples of the ferroelectric domain with the rhombohedral to tetragonal phase transformation and the grain size of the PZT-PZN-PMnN samples of about 2 μm. The SEM images of the domain structure suggest the presence of 90 and 180° domains in the tetragonal phase (**Figure 21(a)**), whereas the 71, 109, and 90° domains are located in the red-bordered region and primarily viewed in **Figure 21(b)**), and the widths of these domains were about 100 nm. Inspection of SEM images acquired at lower magnifications showed that the abundance and scale of these microtwin structures varied with location both within and between ceramic grains, with abrupt changes in the domain structure occurring at the grain boundaries [58]. One of the important contributions from our experimental works is the confirmation of the SEM images by corrosion method as a valid method for domain size assessment in bulk ceramics.

7. Conclusions

This chapter presents the investigation on the fabrication and characterization of sample groups of PZT-based ceramics and the relaxor PZN-PMnN ferroelectric materials with perovskite structure. The B-site oxide mixing technique reported in this study is simple, produces large quantities, and is easy to reproduce. Experimental results showed that the electrical properties of $x\mathrm{Pb}(\mathrm{Zr_yTi_{(1-y)}})\mathrm{O_3}$-$(0.925 - x)\mathrm{Pb}(\mathrm{Zn_{1/3}Nb_{2/3}})\mathrm{O_3}$-$0.075\mathrm{Pb}(\mathrm{Mn_{1/3}Nb_{2/3}})\mathrm{O_3}$ ceramics are optimal at a $\mathrm{Pb}(\mathrm{Zr_yTi_{(1-y)}})\mathrm{O_3}$ content of 0.8 mol and Zr/Ti ratio of 48/52. At these contents, the ceramics have good electrical properties: d_{31} = 140 pC/N, k_p = 0.62, k_t = 0.51, Q_m = 1112, tan δ = 0.005, and P_r = 34.5 μC/cm^2. Investigation of the domain structure of the two ferroelectric phases (tetragonal and rhombohedral) in the PZT-PZN-PMnN with compositions at near the MPB is described as follows: the 90 and 180° domains exist in the tetragonal phase, while 71, 109, and 90° domains are located in the rhombohedral phase. The widths of these domains were about 100 nm. The hysteresis loops of the ceramics exhibited excellent temperature stability due to the broad diffusive phase transition between the nonergodic and

ergodic relaxor states that coexisted over a wide temperature range, which makes it as a promising material for high-intensity ultrasound applications.

Acknowledgements

This research is funded by the Vietnam National Foundation for Science and Technology Development (NAFOSTED) under Grant Number 103.02-2017.308.

Author details

Le Dai Vuong[1*], Vo Thanh Tung[2] and Phan Dinh Gio[2]

1 Faculty of Chemical and Environmental Engineering, Hue Industrial College, Hue City, Vietnam

2 Department of Physics, College of Sciences, Hue University, Vietnam

*Address all correspondence to: ledaivuongqb@gmail.com

References

[1] Huang X, Zeng J, Ruan X, Zheng L, Li G. Structure, electrical, and thermal expansion properties of PZnTe–PZT ternary system piezoelectric ceramics. Journal of the American Ceramic Society. 2018;**101**(1):274-282

[2] Hong C-H, Kim H-P, Choi B-Y, Han H-S, Son JS, Ahn CW, et al. Lead-free piezoceramics – Where to move on? Journal of Materiomics. 2016;**2**(1):1-24

[3] Kour P, Pradhan S, Kumar P, Sinha S, Kar M. Study of ferroelectric and piezoelectric properties on Ca doped PZT ceramics. Materials Today: Proceedings. 2017;**4**(4):5727-5733

[4] Yue Y, Zhang Q, Nie R, Yu P, Chen Q, Liu H, et al. Influence of sintering temperature on phase structure and electrical properties of $0.55Pb(Ni_{1/3}Nb_{2/3})O_3$-$0.45Pb(Zr_{0.3}Ti_{0.7})O_3$ ceramics. Materials Research Bulletin. 2017;**92**:123-128

[5] Qaiser MA, Hussain A, Xu Y, Wang Y, Wang Y, Yang Y, et al. CuO added $Pb_{0.92}Sr_{0.06}Ba_{0.02}(Mg_{1/3}Nb_{2/3})_{0.25}(Ti_{0.53}Zr_{0.47})_{0.75}O_3$ ceramics sintered with Ag electrodes at 900°C for multilayer piezoelectric actuator. Chinese Physics B. 2017;**26**(3):037702

[6] Vuong LD, Gio PD, Tho NT, Chuong TV. Relaxor ferroelectric properties of PZT-PZN-PMnN ceramics. Indian Journal of Engineering & Materials Sciences. 2013;**20**(Dec-2013):555-560

[7] Zhang S, Li F, Jiang X, Kim J, Luo J, Geng X. Advantages and challenges of relaxor-$PbTiO_3$ ferroelectric crystals for electroacoustic transducers – A review. Progress in Materials Science. 2015;**68**:1-66

[8] Irzaman H, Darvina Y, Fuad A, Arifin P, Budiman M, Barmawi M. Physical and pyroelectric properties of tantalum-oxide-doped lead zirconium titanate $[Pb_{0.9950}(Zr_{0.525}Ti_{0.465}Ta_{0.010})O_3]$ thin films and their application for IR sensors. Physica Status Solidi (a). 2003;**199**(3):416-424

[9] Vuong LD, Gio PD, Quang NDV, Dai Hieu T, Nam TP. Development of $0.8Pb(Zr_{0.48}Ti_{0.52})O_3$-$0.2Pb[(Zn_{1/3}Nb_{2/3})0.625(Mn_{1/3}Nb_{2/3})0.375]O_3$ ceramics for high-intensity ultrasound applications. Journal of Electronic Materials. 2018;**47**(10):5944-5951

[10] Vuong LD, Gio PD. Structure and electrical properties of Fe_2O_3-doped PZT-PZN-PMnN ceramics. Journal of Modern Physics. 2014;**5**(14):1258-1263

[11] Vuong LD, Gio PD, Kieu VTT. Raman scattering spectra and dielectric relaxation behavior of PZT-PZN-PMnN ceramics. International Journal of Chemistry and Materials Research. 2014;**2**(6):48-55

[12] Gao F, Cheng L-H, Hong R-Z, Liu J, Wang C-J, Tian C. Crystal structure and piezoelectric properties of $xPb(Mn_{1/3}Nb_{2/3})O_3$–$(0.2-x)Pb(Zn_{1/3}Nb_{2/3})O_3$-$0.8Pb(Zr_{0.52}Ti_{0.48})O_3$ ceramics. Ceramics International. 2009;**35**(5):1719-1723

[13] Tsai C-C, Chu S-Y, Hong C-S, Chen S-F. Effects of ZnO on the dielectric, conductive and piezoelectric properties of low-temperature-sintered PMnN-PZT based hard piezoelectric ceramics. Journal of the European Ceramic Society. 2011;**31**(11):2013-2022

[14] Gio PD, Vuong LD, Hoa HTT. Electrical properties of CuO-doped PZT-PZN-PMnN piezoelectric ceramics sintered at low temperature. Journal of Materials Science and Chemical Engineering. 2014;**2**(11):20-27

[15] Bakhsh N, Khalid F, Hakeem AS, editors. Effect of sintering temperature on densification and mechanical properties of pressureless sintered CNT-alumina nanocomposites. IOP Conference Series: Materials Science and Engineering; 2014: IOP Publishing.

[16] Zheng T, Wu J. Enhanced piezoelectricity over a wide sintering temperature (400-1050 C) range in potassium sodium niobate-based ceramics by two step sintering. Journal of Materials Chemistry A. 2015;**3**(13):6772-6780

[17] Lee G, Ji JH, Koh JH. Enhanced piezoelectric properties of (Bi, Na)TiO_3–(Bi, K)TiO_3 ceramics prepared by two-step sintering process. International Journal of Applied Ceramic Technology. 2018;**15**(2):531-537

[18] Vuong LD, Truong-Tho N. Effect of ZnO nanoparticles on the sintering behavior and physical properties of $Bi_{0.5}(Na_{0.8}K_{0.2})_{0.5}TiO_3$ lead-free ceramics. Journal of Electronic Materials. 2017;**46**(11):6395-6402

[19] Vuong LD, Tho NT. The sintering behavior and physical properties of Li_2CO_3-doped $Bi_{0.5}(Na_{0.8}K_{0.2})0.5TiO_3$ lead-free ceramics. International Journal of Materials Research. 2017;**108**(3):222-227

[20] Wang J, Wang G, Nie H, Chen X, Cao F, Dong X, et al. Low-temperature sintering and electric properties of $Pb_{0.99}(Zr_{0.95}Ti_{0.05})0.98Nb_{0.02}O_3$ ferroelectric ceramics with CuO additive. Journal of the American Ceramic Society. 2013;**96**(8):2370-2373

[21] Kang SH, Ahn CW, Lee HJ, Kim IW, Park EC, Lee JS. Dielectric and pyroelectric properties of Li_2CO_3 doped $0.2Pb(Mg_{1/3}Nb_{2/3})O_3$-$0.5Pb(Zr_{0.48}Ti_{0.52})O_3$-$0.3Pb(Fe_{1/3}Nb_{2/3})O_3$ ceramics. Journal of Electroceramics. 2008;**21**(1-4):855-858

[22] Yoo J, Lee I, Paik DS, Park Y-W. Piezoelectric and dielectric properties of low temperature sintering $Pb(Mn_{1/3}Nb_{2/3})O_3$–$Pb(Zn_{1/3}Nb_{2/3})O_3$–$Pb(Zr_{0.48}Ti_{0.52})O_3$ ceramics with variation of sintering time. Journal of Electroceramics. 2009;**23**(2-4):519-523

[23] Kim Y-J, Yoo J, Lee J-Y. Piezoelectric properties of PCW-PNN-PZT ceramics sintered at low temperature. Ferroelectric Letters Section. 2017;**44**(1-3):1-7

[24] Yoon M-S, Kim Y-M, Kweon S-Y, Hong T-W, Lee Y-G, Ryu S-L, et al. Effects of ZnO on the piezoelectric properties of Pb $(Mn_{1/3}Sb_{2/3})O_3$-$Pb(Zr, Ti)O_3$ ceramics. Journal of Electroceramics. 2007;**18**(1-2):73-75

[25] Yuhuan X. Ferroelectric Materials and Their Applications. North Holland; 1991

[26] Vuong LD, Gio PD, Lien NTK. Physical properties of PZT-PZN-PMnN ceramics were fabricated by B-site oxide mixing technique. Hue University Journal of Science (HU JOS). 2013;**84**(6):93-99

[27] Fang B, Sun R, Shan Y, Tezuka K, Imoto H. On the feasibility of synthesizing complex perovskite ferroelectric ceramics via a B-site oxide mixing route. Journal of Materials Science. 2007;**42**(22):9227-9233

[28] Tsai C-C, Chu S-Y, Liang C-K. Low-temperature sintered PMnN-PZT based ceramics using the B-site oxide precursor method for therapeutic transducers. Journal of Alloys and Compounds. 2009;**478**(1-2):516-522

[29] Lee S-H, Yoon C-B, Lee S-M, Kim H-E. Reaction sintering of lead zinc niobate–lead zirconate titanate ceramics. Journal of the European Ceramic Society. 2006;**26**(1-2):111-115

[30] Necira Z, Boutarfaia A, Abba M, Menasra H, Abdessalem N. Effects

of thermal conditions in the phase formation of undoped and doped Pb(Zr1-xTix)O_3 solid solutions. Materials Sciences and Applications. 2013;**4**(05):319-323

[31] Fan H, Kim HE. Effect of lead content on the structure and electrical properties of Pb((($Zn_{1/3}Nb_{2/3}$)0.5($Zr_{0.47}Ti_{0.53}$)0.5)O_3 ceramics. Journal of the American Ceramic Society. 2001;**84**(3):636-638

[32] Kwok KW, Chan HLW, Choy CL. Evaluation of the material parameters of piezoelectric materials by various methods. IEEE Transactions on Ultrasonics, Ferroelectrics, and Frequency Control. 1997;**44**(4):733-742

[33] Baghai-Wadji A, Gharb NB, Bouakaz A, Damjanovic D, Dayton P, Degertekin L, et al. IEEE ultrasonics, ferroelectrics, and frequency control society. Aurora. 1987;**51**:60504

[34] Sawyer CB, Tower C. Rochelle salt as a dielectric. Physical Review. 1930;**35**(3):269

[35] Lee S-H, Kim H-G, Choi H-I, Sa-Gong G, editors. Dielectric and piezoelectric properties of PNN-PZN-PZT ceramics for actuator application. In: Proceedings of the 5th International Conference on Properties and Applications of Dielectric Materials; 1997. IEEE; 1997

[36] Halliyal A, Safari A. Synthesis and properties of lead zinc niobate: Pb($Zn_{1/3}Nb_{2/3}$)O_3 based relaxor ferroelectrics. Ferroelectrics. 1994;**158**(1):295-300

[37] Pakawanit P, Ngamjarurojana A, Prasatkhetragarn A, Ananta S. Characterization of 0.93Pb($Zn_{1/3}Nb_{2/3}$)O_3-0.07$BaTiO_3$ ceramics derived from a novel $Zn_3Nb_2O_8$ B-site precursor. Ceramics International. 2013;**39**:S325-S329

[38] Fan H, Kim H-E. Perovskite stabilization and electromechanical properties of polycrystalline lead zinc niobate–lead zirconate titanate. Journal of Applied Physics. 2002;**91**(1):317-322

[39] Seo SB, Lee SH, Yoon CB, Park GT, Kim HE. Low-temperature sintering and piezoelectric properties of 0.6Pb($Zr_{0.47}Ti_{0.53}$)$O_3$0.4Pb($Zn_{1/3}Nb_{2/3}$)O_3 ceramics. Journal of the American Ceramic Society. 2004;**87**(7):1238-1243

[40] Vittayakorn N, Rujijanagul G, Tunkasiri T, Tan X, Cann DP. Perovskite phase formation and ferroelectric properties of the lead nickel niobate–lead zinc niobate–lead zirconate titanate ternary system. Journal of Materials Research. 2003;**18**(12):2882-2889

[41] Hou Y-D, Chang L-M, Zhu M-K, Song X-M, Yan H. Effect of Li_2CO_3 addition on the dielectric and piezoelectric responses in the low-temperature sintered 0.5 PZN–0.5 PZT systems. Journal of Applied Physics. 2007;**102**(8):084507

[42] Yogaraksa T, Hikam M, Irzaman H. Rietveld analysis of ferroelectric $PbZr_{0.525}Ti_{0.475}O_3$ thin films. Ceramics International. 2004;**30**(7):1483-1485

[43] Prakash BJ, Buddhudu S. Synthesis and analysis of $LiNbO_3$ ceramic powders by co-precipitation method. Indian Journal of Pure and Applied Physics. 2012;**320-324**(5):320-324

[44] Uchino K. Relaxor ferroelectrics. Journal of the Ceramic Society of Japan. 1991;**99**(1154):829-835

[45] Rubio-Marcos F, Romero J, Martín-Gonzalez M, Fernández J. Effect of stoichiometry and milling processes in the synthesis and the piezoelectric properties of modified KNN nanoparticles by solid state reaction. Journal of the European Ceramic Society. 2010;**30**(13):2763-2771

[46] Dixit A, Majumder S, Dobal P, Katiyar R, Bhalla A. Phase transition studies of sol–gel deposited barium zirconate titanate thin films. Thin Solid Films. 2004;**447**:284-288

[47] Kahoul F, Hamzioui L, Boutarfaia A. The influence of Zr/Ti content on the morphotropic phase boundary and on the properties of PZT–SFN piezoelectric ceramics. Energy Procedia. 2014;**50**:87-96

[48] Vuong LD, Gio PD. Enhancement in dielectric, ferroelectric, and piezoelectric properties of $BaTiO_3$-modified $Bi_{0.5}(Na_{0.4}K_{0.1})TiO_3$ lead-free ceramics. Journal of Alloys and Compounds. 2020;**817**:152790

[49] Yoo J, Lee Y, Yoon K, Hwang S, Suh S, Kim J, et al. Microstructural, electrical properties and temperature stability of resonant frequency in $Pb(Ni_{1/2}W_{1/2})O_3$–$Pb(Mn_{1/3}Nb_{2/3})O_3$–$Pb(Zr, Ti)O_3$ ceramics for high-power piezoelectric transformer. Japanese Journal of Applied Physics. 2001;**40**(5R):3256-3259

[50] Vuong LD, Gio PD, Van Chuong T, Trang DTH, Hung DV, Du NT. Effect of Zr/Ti ratio content on some physical properties of low temperature sintering PZT–PZN–PMnN ceramics. International Journal of Materials and Chemistry. 2013;**3**(2):39-43

[51] Jaita P, Sanjoom R, Lertcumfu N, Rujijanagul G. Improvement of electric field-induced strain and energy storage density properties in lead-free BNKT-based ceramics modified by BFT doping. RSC Advances. 2019;**9**(21):11922-11931

[52] Fan H, Zhang L, Zhang L, Yao X. The effect of defect field on dielectric ageing of lead magnesium niobate-lead titanate relaxor ferroelectrics. Journal of Physics: Condensed Matter. 2000;**12**(19):4381-4390

[53] Luan NDT, Vuong LD, Van Chuong T, Truong TN. Structure and physical properties of PZT-PMnN-PSN ceramics near the morphological phase boundary. Advances in Materials Science and Engineering. 2014;**2014**(821404):8

[54] Truong-Tho N, Vuong LD. Effect of sintering temperature on the dielectric, ferroelectric and energy storage properties of SnO_2-doped $Bi_{0.5}(Na_{0.8}K_{0.2})_{0.5}TiO_3$ lead-free ceramics. Journal of Advanced Dielectrics. 2020;**10**(4):2050011-2050019

[55] Li H-B, Li Y, Wang D-W, Lu R, Yuan J, Cao M-S. Effects of ZnO nanoneedles addition on the mechanical and piezoelectric properties of hard PZT-based composites. Journal of Materials Science: Materials in Electronics. 2013;**24**(5):1463-1468

[56] German RM. Liquid Phase Sintering. Springer Science & Business Media; 2013

[57] Luo CY, Hu MZ, Huang Q, Fu Y, Gu HS. Influence of ZnO and Nb_2O_5 additions on sintering behavior and microwave dielectric properties of $(Mg_{0.95}Ca_{0.05})TiO_3$ ceramics. Key Engineering Materials. 2012;**512**:1184-1188

[58] Rossetti GA Jr, Popov G, Zlotnikov E, Yao N. Domain structures and nonlinear mechanical deformation of soft $Pb(Zr_xTi_{1-x})O_3$ (PZT) piezoelectric ceramic fibers. Materials Science and Engineering A. 2006;**433**(1-2):124-132